LETTER
SPACE PHYSICS

Earth and Planetary Physics
2: 479–488, 2018
doi: 10.26464/epp2018046

The Langmuir Probe onboard CSES: data inversion analysis method and first results

Rui Yan[1]*, YiBing Guan[2], XuHui Shen[1], JianPing Huang[1], XueMin Zhang[3], Chao Liu[2], and DaPeng Liu[1]

[1]The Institute of Crustal Dynamics, China Earthquake Administration, Beijing 100085, China;

[2]National Space Science Center, China Earthquake Administration, Beijing 100190, China;

[3]The Institute of Earthquake Forecasting, China Earthquake Administration, Beijing 100036, China

Abstract: The Langmuir Probe (LAP), onboard the China Seismo-Electromagnetic Satellite (CSES), has been designed for *in situ* measurements of bulk parameters of the ionosphere plasma, the first Chinese application of *in-situ* measurement technology in the field of space exploration. The two main parameters measured by LAP are electron density and temperature. In this paper, a brief description of the LAP and its work mode are provided. Based on characteristics of the LAP, and assuming an ideal plasma environment, we introduce in detail a method used to invert the I-V curve; the data products that can be accessed by users are shown. Based on the LAP data available, this paper reports that events such as earthquakes and magnetic storms are preceded and followed by obvious abnormal changes. We suggest that LAP could provide a valuable data set for studies of space weather, seismic events, and the ionospheric environment.

Keywords: Langmuir Probe (LAP); Current-Voltage (I-V) curve; electron density (N_e); electron temperature (T_e)

Citation: Yan, R., Guan, Y. B., Shen, X. H., Huang, J. P., Zhang, X. M., Liu, C., and Liu, D. P. (2018). The Langmuir Probe onboard CSES: data inversion analysis method and first results. *Earth Planet. Phys.*, *2*(6), 479–488. http://doi.org/10.26464/epp2018046

1. Introduction

Perturbations in ionospheric plasma parameters have been observed before many large earthquakes. New spacecraft and payload technology provide a significant opportunity to study further the potential for space observations to predict earthquakes (Zhao GZ et al., 2007). Langmuir probes have been extensively used in space plasma diagnostics for more than 40 years (Brace et al., 1971; Bering et al., 1973), having been included in the payloads of spacecraft of many countries (Holback et al., 2001; Eriksson et al., 2007). In particular, the Langmuir probe on the French DEMETER satellite has played an important role in the field of seismic monitoring research (Lebreton et al., 2006). From its records, many ionospheric plasma perturbations related to seismic events have been detected (Sarkar et al., 2007, 2012; Zhang XM et al., 2010a, b; Liu J et al., 2011). Furthermore, statistical analysis of plasma parameters has been developed to ascertain the relationships between ionospheric perturbations and large earthquakes (He Y et al., 2010, 2011; Parrot, 2012; Píša et al., 2011; Li M and Parrot, 2012; Yan R et al., 2017a).

The China Seismo-Electromagnetic Satellite (CSES), also called ZHANGHENG-1, was launched sucessfully on February 2, 2018 (Shen XH et al., 2018). The Langmuir probe onboard the CSES, called "LAP", is China's first application of *in-situ* measurement technology in the field of space exploration.

CSES is the first space-based platform in China for both earthquake observation and geophysical field measurement, and is the first satellite of China's space-based geophysical field observation system. It has considerable potential to contribute valuable new data to such fields as earthquake science, geophysics, and space sciences (Shen XH et al., 2018). The CSES is a Sun-synchronous satellite orbiting at a height of 500 km with a descending node of 14:00 local time. Its scientific payloads include a search-coil magnetometer, an electric field detector, a high precision magnetometer, a plasma analyzer package, a Langmuir probe, an energetic particle detector, a GNSS occupation receiver, and a three-frequency beacon (Shen XH et al., 2018). Of these, the Langmuir probe (LAP) and plasma analyzer package (PAP) are the space plasma in-situ detection payloads (Liu C et al., 2018). The scientific objective of the Langmuir probe is to study space plasma physics phenomena and ionospheric changes caused by seismic events, magnetic storms, etc. The payloads need to have a range of measurement sufficiently broad to cover the maximum range of plasma changes at the 500 km altitude, and sufficiently high accuracy to identify weak abnormal information (Liu C et al., 2018). The LAP can measure electron density (N_e) over a range from 5×10^2~1×10^7 cm^{-3}, and electron temperature (T_e) from 500 K to 10,000 K with relative measurement accuracy of 10%. It is also capable of monitoring the spacecraft potential and its variations.

In Section 2 we describe in brief the LAP instrument design and provide an overview of its operations modes. In Section 3 we present the data analysis method. Examples of preliminary LAP

Correspondence to: R. Yan, yanxiaoxiao_best@163.com
Received 18 AUG 2018; Accepted 18 OCT 2018.
Accepted article online 05 NOV 2018.

scientific results are described in Section 4. Concluding remarks are given in Section 5.

2. The LAP Instrument Description and Operation Mode

A Langmuir Probe, in its simple form, is a conductor immersed in plasma to which a bias voltage is applied. The principle of the measurement technique is to vary the bias voltage and to measure the current collected as a function of the applied voltage, i.e. to acquire the current-voltage (I-V) characteristic of the probe (Chen FF and Chang JP, 2002; Guan YB et al., 2011).

The LAP onboard the CSES consists of Sensor 1, Sensor 2 and an electronics box (Figure 1). Sensor 2 is designed as a backup. Sensor 1 has a diameter of 5 cm; Sensor 2 has a diameter of 1 cm. Both sensors are immersed in the plasma by extension bars. The sensor extension bar, whose length is 50 cm, is designed to support the sensor away from the satellite surface and to reduce the interference of the satellite (Guan YB et al., 2011). The sensors are given bias voltage, controlled by the electronics box, the principal components of which are a sweep voltage circuit, a sensor signal output circuit, a control and processing circuit, the satellite interface circuit, and a power supply circuit. The sweep voltage circuit is operated by the control and processing unit which generates a continuous sweep voltage loaded to the sensor, by controlling the digital-to-analog convert circuit. The sensor signal output circuit is designed to collect and convert the sensor current signal by the preamplifier circuit and the differential circuit (Liu G et al., 2018; Guan YB et al., 2011).

When the satellite is in orbit, the satellite body and the extended strut form plume in the opposite direction of the satellite flight direction. The detection region of the LAP must avoid the plume because it disturbs the space plasma and causes errors in measurement. The LAP has been installed on the front of satellite. Design of the LAP on the CSES is described in more detail in previous reports (Guan YB et al., 2011; Liu C et al., 2016, 2018).

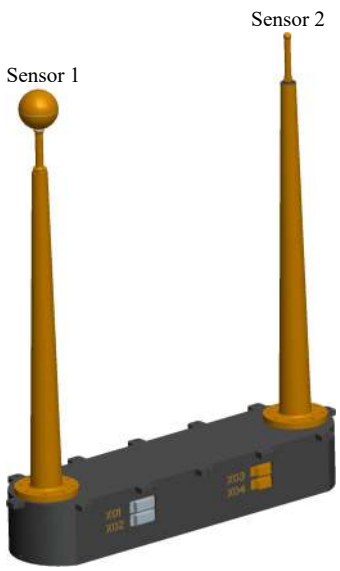

Figure 1. Configuration of the LAP (Liu C et al., 2018).

When a conductor immersed in plasma is biased, it acquires a space charge based on the relative flux of electrons and ions to the conductor. When the bias voltage is negative, the probe collects an ion current and repels electrons from the ambient plasma. Conversely, for a positive voltage, it collects an electron current and repels ions. The response of the LAP is obtained by acquiring the I-V characteristic.

When the area of a sensor is fixed, the effect of a satellite ground potential will increase with increasing scanning voltage amplitude. The current collected by Sensor 1 (5 cm) would be much larger than Sensor 2 (1 cm) because of its larger collecting area, which make it easier to get current. Because Sensor 1 is relatively large compared to the size of the satellite, if the positive biased voltage applied to Sensor 1 is too large, the spacecraft's ground potential could be lowered by the Sensor 1's relatively high collected electron current (Szuszczewicz, 1972). Conversely, Sensor 2 is small enough compared to the satellite that its collected current would have nearly no effect on the ground potential of the spacecraft, even when a relatively large positive voltage is applied to Sensor 2. But it is somewhat difficult to measure very low plasma densities. So the sweeping voltage (V_s) is −3 V–+3 V for Sensor 1, and −6 V–+6 V for Sensor 2 (Guan YB et al., 2011). The +3 V bias loading on Sensor 1 causes a 0.05 V decrease in the satellite potential, which can be ignored. When the load on Sensor 2 is +6 V bias, the satellite potential decreases by less than 0.01 V, which has an insignificant effect on the satellite's potential (Liu C et al., 2016).

The operational modes of the LAP include *survey mode* and *burst mode*. The survey mode is used mainly to detect global electron density and electron temperature, while the burst mode primarily allows detection of key areas, over China and within seismic belts, because bursts can yield physical parameters in greater detail. We can obtain an I-V curve from a set of whole voltage sweepings. In order to compare different states, each sweeping period contains 3 parts: voltage down-sweeping, voltage up-sweeping and fixed bias voltage sweeping. The sweeping period for the burst mode is 1.5 seconds: 0.5 s for the voltage down-sweeping, 0.5 s for the voltage up-sweeping, and 0.5 s for the fixed bias voltage (Figure 2). The sweeping period for the survey mode is 3 seconds: 1 s for the down-sweeping, 1 s for the up-sweeping, and 1 s for the fixed bias voltage.

For fixed bias voltage sweeping, the LAP measures the collected currents only in the saturation regions by applying a fixed voltage relative to the spacecraft ground. In a short time, the electron temperature can be assumed to be constant, and the electron density is directly proportional to the electron current; that is, the relative plasma density fluctuation can always be estimated from the current variations of the probe. The advantage of the fixed biased probe is the high resolution of its measurements, while the disadvantage is that it cannot measure the electron temperature, nor the absolute electron density but only relative variation of electron density (Guan YB et al., 2011), so N_e/T_e cannot be calculated from fixed bias voltage sweeping. From each complete voltage down-sweeping and up-sweeping, we can get an I-V curve and then an electron density (N_e) and electron temperature (T_e). However, the voltage down-sweeping is subject to interfer-

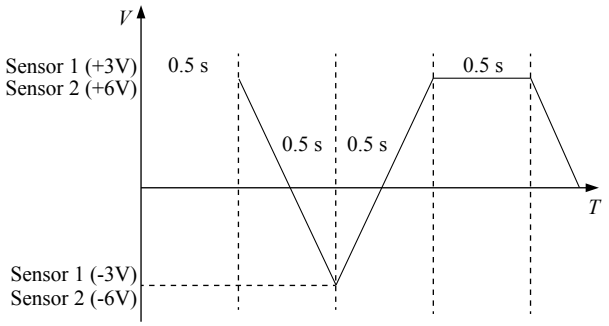

Figure 2. The voltage sweeping cycle of LAP in burst mode.

ence. So we calculate N_e/T_e only from up-sweeping; the result from down-sweeping is used as verification. Therefore, because the velocity of the satellite is 7.8 km/s and the resolution of LAP in survey mode is 3 seconds, spatial resolution on the 500 km altitude CSES orbit is approximately 24 km; in burst mode, time resolution is 1.5 seconds, corresponding to about 12 km spatial resolution.

3. Data Inversion Analysis Method and Data Product

Before the CSES was launched, we studied the data analysis method carefully and set some primarily parameters in the inversion process; the method was verified using data from plasma chamber testing in INFN-IAPS (National Institute for Astrophysics -Institute for Space Astrophysics and Planetology) (Yan R et al., 2017b). Now that CSES has been launched successfully, we apply the method to actual observation data. In this section, we review the basic theory that govern characteristics of the I-V curve and introduce the analysis method applied to data from the LAP on CSES. We also introduce the data base that can be accessed by researchers.

3.1 Data Inversion Analysis Method

A typical I-V characteristic in both linear-linear and linear-log scale is shown in Figure 3, which contain three main regions (the ion saturation region, the electron retardation region, and the electron saturation region) and two important data points (floating potential (V_f) and plasma potential (V_p)) (Hutchinson, 1987; Chen FF and Chang JP, 2002). The V_f is where the ion and electron currents are equal and the net current is zero. The V_p is near the cross point of electron retardation and electron saturation, where all the electrons have been repelled and only the ion saturation current is detected. In the transition region, the ion current is negligible, and the electrons are partially repelled by the negative potential. In a Maxwellian plasma, this part of the curve is changing exponentially; when the sweeping voltage reaches V_p, all of the random thermal flux of electrons is collected. In the electron saturation region, electron current grows slowly because of the expansion of the sheath.

Irving Langmuir first proposed the concept of what is now known as a Langmuir probe, and then together with Mott-Smith, gave the classical theoretical formula under the approximate conditions of a Langmuir probe, applying the Orbit-Motion-Limited (OML) theory (Langmuir et al., 1924, 1932; Mott-Smith et al., 1961). The principal theory of the Langmuir probe is well established, when plasma conditions are such that the Debye Length is much larger than the dimensions of the electrode (Lebreton et al., 2006). In data inversion, we only consider the current contribution from the background plasma electrons and ions. The effects of the photoelectrons, of secondary emission and of the magnetic field are not considered. According to the theoretical Langmuir probe formula (Langmuir and Mott-Smith, 1924; Langmuir, 1932; Mott-Smith, 1961), the electron density and electron temperature of the plasma are obtained by fitting the I-V characteristic curve.

The raw data of the LAP contains all sweep voltage values (V_{scan}), output voltage value (V_{out}) and range information (R). Data calibration aims to convert the output voltage corresponding to the scanning voltage into the collection current, and then we can obtain the I-V curve. Based on the linear amplifying circuit, the linear relationship between current and voltage is shown in equation (1):

$$I = a_j V_{out} + b_j, \tag{1}$$

where, V_{out} is output voltage, I is collected current, a_j is gain coefficient, b_j is drift in zero, and j = 1, 2, 3, represent three different

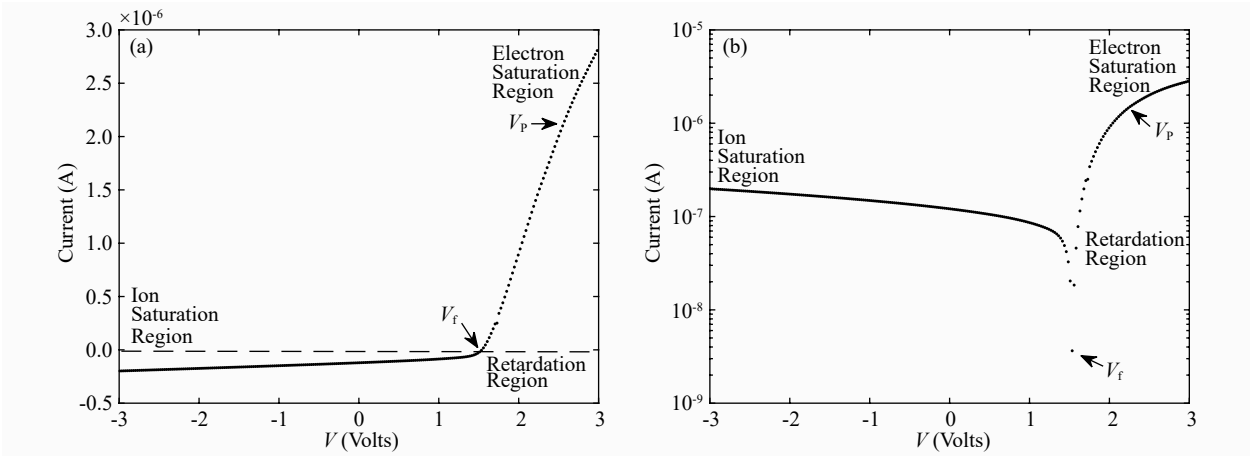

Figure 3. Typical I-V characteristic of LAP (in orbit 2661 during 2018-02-19, 18:38:57–2018-02-19, 19:09:14). In both plots, the bias voltage is on a linear scale. (a) The current is on a linear scale; (b) The current is on a logarithm scale.

ranges, respectively. Gain coefficient and drift in zero is different according to range information.

Then we obtained a whole I-V curve and N_e/T_e are obtained from the I-V characteristics. The main steps are:

(1) When electron current (I_e) is equal to the ion current (I_i), the sweep voltage value is the floating potential (V_f). So the floating potential (V_f) is identified when the total collected current is 0.

(2) In theory, the ion saturation region is in the range of $V \leqslant V_f - \frac{5kT_{ec}}{e}$ (Chen FF and Chang JP, 2002). The initial electron temperature (T_{ec}) in the ionosphere is here set at 3000 K. We derived an approximation curve (I_i) for the ion saturation region, and then derived ion current approximation curves in the electron retardation and electron saturation regions.

(3) Subtracting the ion approximation current (I_i) from the total electron current (I), gives the electron current (I_e), that is $I_e=I-I_i$.

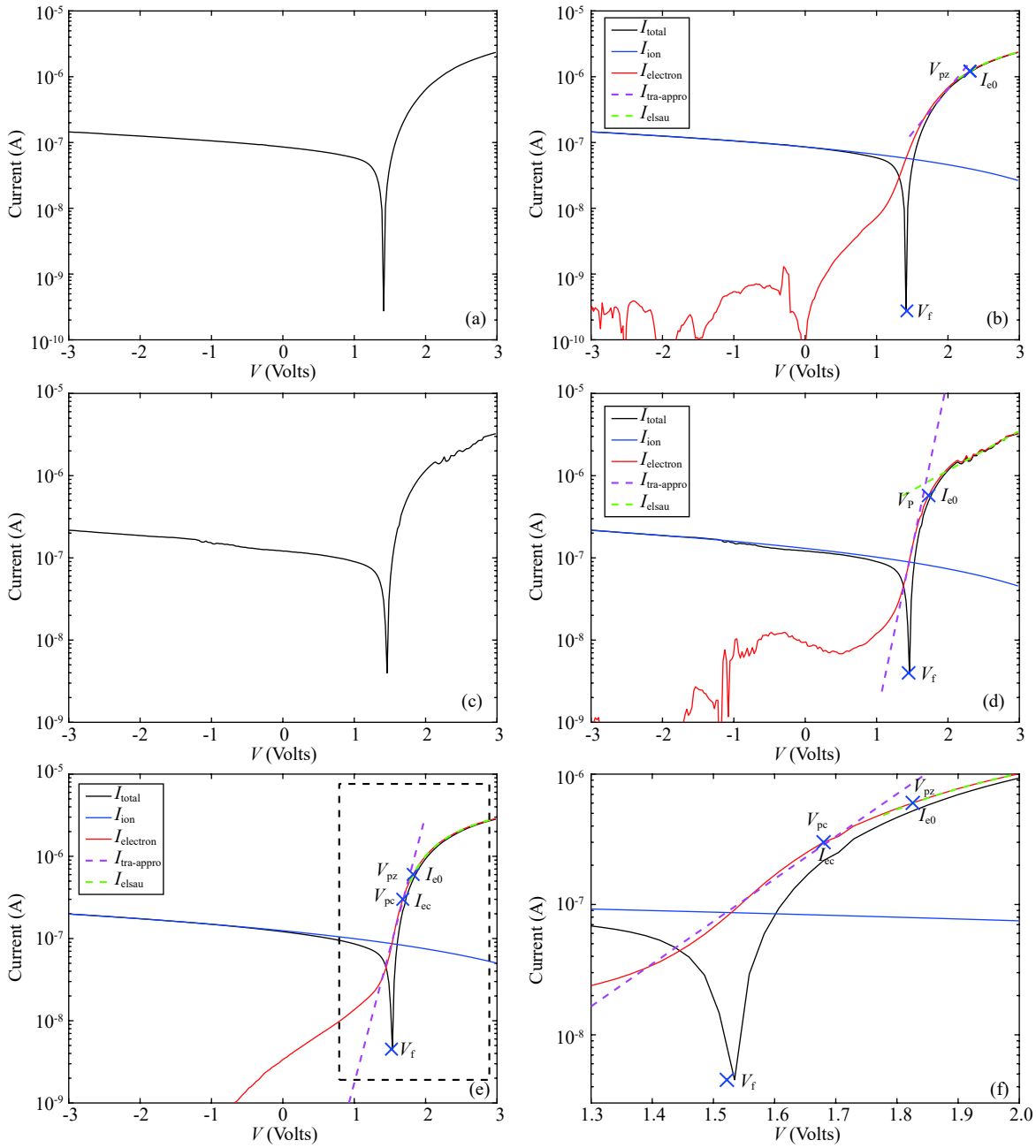

Figure 4. The data inversion analysis for different I-V curve in orbit 2661. (a) is the smooth I-V curve, (b) is the characteristics analysis process of (a), V_p can be determined using the second derivative $I''(V)$ directly; (c) is special I-V curves with many fluctuations, (d) is characteristics analysis process of (c), V_p can be obtained from the point at which the slope of the electron retardation region crosses the approximation curve for the electron saturation region; (e) is the characteristics analysis process of an I-V curve with several fluctuation near the inflection point of electron retardation and electron saturation, (f) is the local amplification of (e), V_p should be reconfirmed by iteration.

(4) Next we identify the plasma potential (V_p). V_p is the inflection point of the electron retardation region and electron saturation region. For the normal smooth I-V curve (Figure 4(a, b)), we determine V_p using the second derivative $I''(V)$. But for the special I-V curve that may be affected by the satellite or unknown interference, there are some fluctuations, especially in the electron saturation and electron retardation regions (Figure 4c). In this case, the V_p point cannot be determined by the second derivative $I''(V)$. However, V_p can be obtained from the point at which the slope of the electron retardation region crosses the approximation curve for the electron saturation region (Figure 4d). The time-honored way to obtain the space potential (or plasma potential) is to draw straight lines through the I-V curve in the transition and electron saturation regions and call the crossing point V_p. This does not work well if the electron retardation region is curved. In this case, taking the point where I_e starts to deviate from exponential growth is a good method (Chen FF and Chang JP, 2002; Godyak and Alexandrovich, 2015). So for the special I-V curve with some fluctuations, finding the crossing of the slope of the electron retardation region and of the approximation curve for the electron saturation region is the relatively best choice.

(5) We next reconfirm V_p by iteration if needed. A measurement error in the plasma potential can lead to an order of magnitude error in finding the electron saturation current and, correspondingly, in the calculated electron density. An error in determining the electron temperature can be even more significant (Godyak and Alexandrovich, 2015). Some I-V curves may have few fluctuations, as in Figure 4, but may not be completely smooth. Figure 4e is the characteristics analysis process of a whole I-V curve, and Figure 4f is the local amplification near the inflection point of electron retardation and electron saturation in Figure 4e. From Figure 4f we can see more clearly that there is a fluctuation near the inflection point (arrow position). So V_p obtained by the second derivative is just the fluctuation position. In this case, we can't find the exact V_p point from a single second derivative; iteration is needed. The steps are: take V_p obtained by Step (4) as V_{p1} ; setting V_{p1} and V_f as boundaries, we can get the new ion saturation, electron retardation, and electron saturation region; then we find the crossing point of the slope of the electron retardation region and of the approximation curve for the electron saturation region; this crossing point is V_{p2}. Repeating the previous procedure, we set V_{p2} and V_f as the boundaries of the ion saturation, electron retardation, and electron saturation region and the find the new crossing point of these two new regions. Then set it as V_{p3}, and so forth. When (V_{pn}–$V_{p(n-1)}$) is minimized, V_{pn} is the final V_p.

In general, 2 or 3 iterations are often sufficient. When the I-V curve is smooth (Figure 4(a, b)) or exhibits few fluctuations (Figure 4(e, f)), the approximation curve for the electron saturation region can be calculated by curve fitting; for special I-V curves with many fluctuations (Figure 4(c, d)), good results can be obtained simply by linear fitting.

(6) The electron retardation region is the exponential part of the I-V curve; when plotted semi-logarithmically, the sweeping voltage and current should be a straight line if the electrons are Maxwellian (Hutchinson, 1987; Chen FF and Chang JP, 2002):

$$I_e = I_{e0}\exp\left(\frac{eV}{kT_e}\right), \tag{2}$$

$$\ln I_e = \ln I_{e0} + \frac{eV}{kT_e}. \tag{3}$$

Equation (3) shows that the slope ($\tan\varphi$) of the ($\ln I_e$)-V curve is exactly proportional to $1/T_e$ and is a good measure of the electron temperature. So T_e can be derived by applying equation (4):

$$T_e = \frac{e}{k\times\tan\varphi} \approx \frac{11600}{\tan\varphi}. \tag{4}$$

(7) The electron current (I_{e0}) at V_p point is determined from the I-V curve and the N_e is derived by applying equation (5):

$$N_e = \frac{I_{e0}}{e\times A}\sqrt{\frac{2\pi m_e}{kT_e}}. \tag{5}$$

In all the above equations, k is 1.38×10^{-23} (boltzman constant); e is 1.6×10^{-19} (coulomb charge); m_e is 9.1×10^{-31} (the electron mass); A is the deployed area of the probe.

3.2 Data Representation

The CSES provides a total of five levels of data (Shen XH et al., 2018). For the LAP, Level 0 is the raw data (sweep voltage values, output voltage values, and range information) generated after a series of processes including frame synchronization, de-randomization, decoding, and de-formatting; Level 1 is the data (electron density, electron temperature, floating voltage, and plasma voltage) obtained after general error rejection, format conversion, and calibration of Level 0 data. Level 2 is physical quantity data (electron density, electron temperature, floating voltage, and plasma voltage) with satellite orbit information after coordination system transformation and necessary data inversion of Level 1 data. Level 3 is time-sequential data (electron density, electron temperature) in the frame of satellite orbits, generated after resampling. Level 4 is global or regional dynamic observation data (electron density, electron temperature) retrieved from Level 2 and Level 3 data, in terms of variation between recursive orbits and disturbances observed according to the background field.

After finishing the in-orbit test, the user can have access to Level 2 science data by connecting to the CSES website. We present one example of Level 2 data in Figure 5, including descending orbit and ascending orbit. The first panel represents the variation of the probe's floating potential and of the plasma potential measured by Sensor 1 of the LAP. The second and third panels, respectively, are derived electron density and electron temperature. The latitude, longitude, universal time, and Beijing time are marked below these data.

4. Preliminary LAP Science Results

The CSES is currently in commission phase; some experiments and tests are being conducted. But we have been able to acquire some useful data. Several specific features, such as magnetic storms and variations related to earthquakes have been observed. These observations are described here to illustrate the measurement capabilities of the LAP.

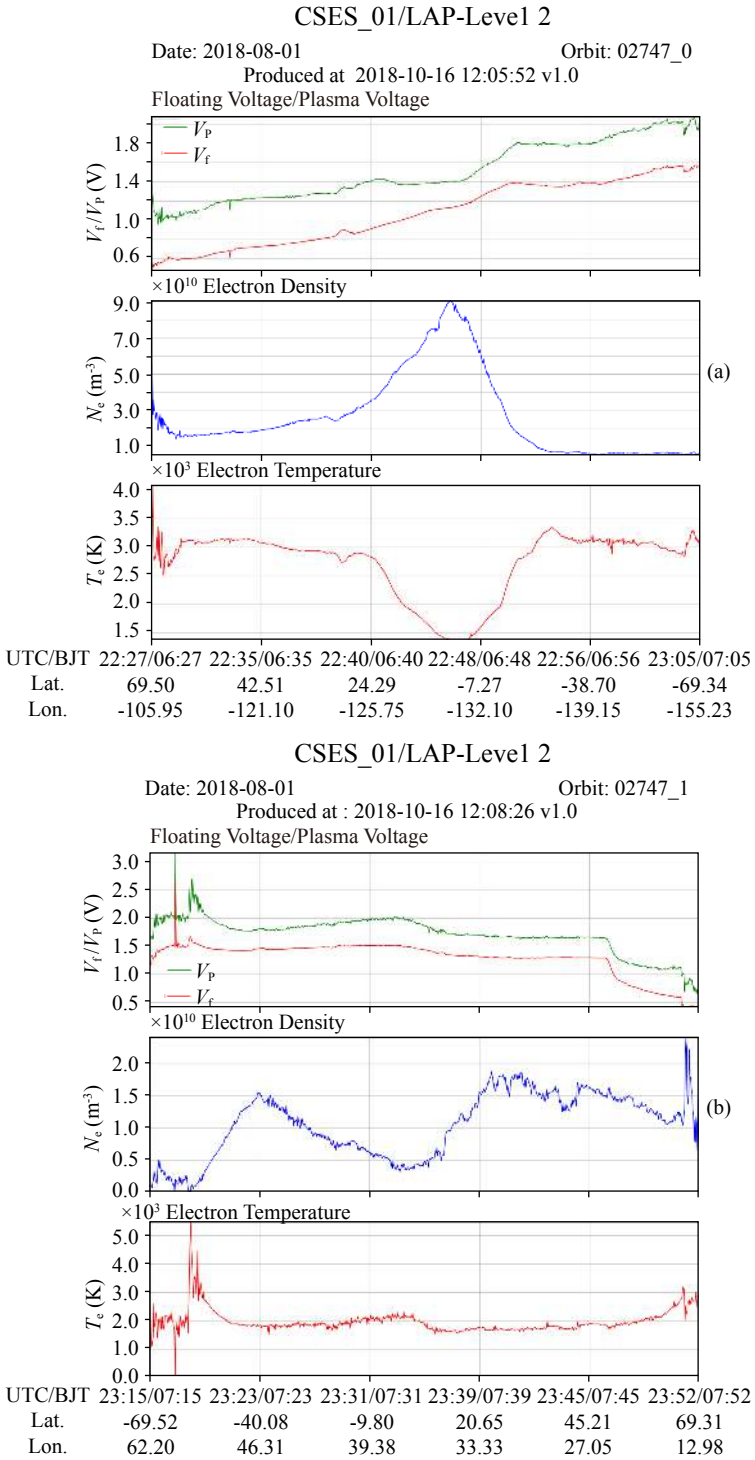

Figure 5. LAP level 2 data. (a) is descending orbit; (b) is ascending -orbit.

4.1 Magnetic Storm

A magnetic storm is a complex process that originates from solar wind and the magnetosphere. It can cause severe global ionospheric disturbance and affect the neutral atmosphere, including the troposphere and the middle atmosphere. During magnetic storms, some ionospheric parameters exhibit drastic changes (Yao YB et al., 2013). We present data regarding the magnetic storm on the 1st of June. (Figure 6).

According to *Kp* index records every 3 hours on 1st June (Table 1), the *Kp* index during 13:00–15:00 was 5, the maximum. In this paper, the data during this time range is selected and tracked forward and backward respectively by revisited orbits (Figure 7) (revisited orbits are the orbits passing by the same sub-satellite point, which means these revisited orbits are roughly above the same location). We compared the N_e at the same position (revisited orbit) and same time before and after the magnetic storm. Three groups of data from revisited orbits were selected separ-

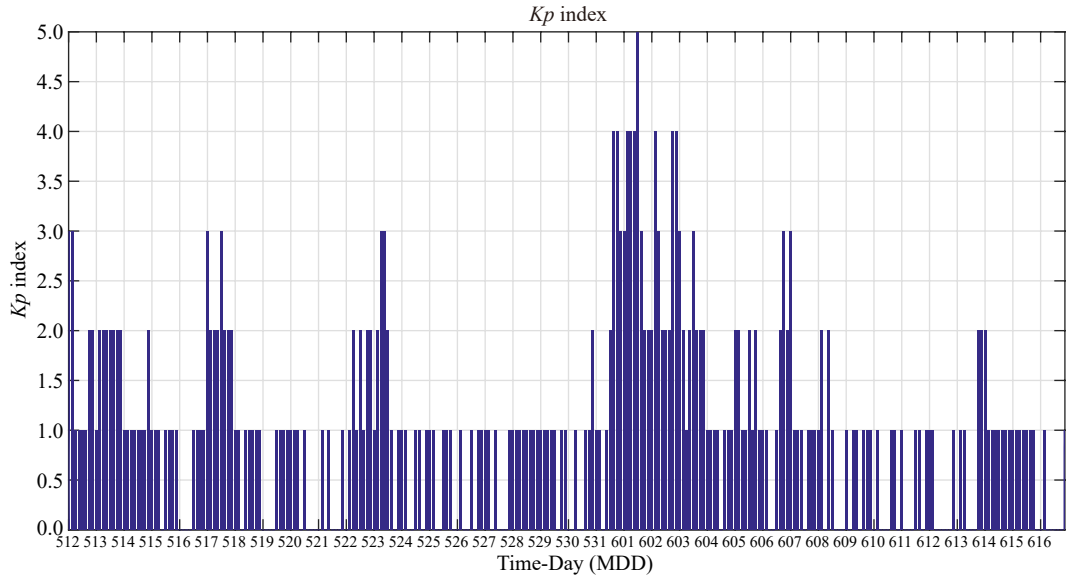

Figure 6. Planetary magnetic 3 hour *Kp* indices (https://www.gfz-potsdam.de/en/kp-index).

Table 1. *Kp* index records every 3 hours before and after magnetic storm in 1 June

	00:00–03:00	04:00–06:00	07:00–09:00	10:00–12:00	13:00–15:00	16:00–18:00	19:00–21:00	22:00–24:00
18:05:12	3	3	1	1	1	1	2	2
18:05:17	3	2	2	2	3	2	2	2
18:05:22	0	1	2	1	2	1	2	2
18:05:27	1	1	0	1	0	0	0	1
18:06:01	**3**	**4**	**4**	**4**	**5**	**3**	**2**	**2**
18:06:06	1	1	0	0	1	2	3	2
18:06:16	0	1	0	0	0	0	0	1

ately on the night side and the day side, in the main phase of this storm. The local time of the night side was about 02:00, and of the day side was approximately 14:00. Tracked data from 12, 17, 22, 27 May are references for quiet periods before the magnetic storm; tracked data from 6 and 16 June are quiet references after the storm (There are no data during this time range from 11 June). The *Kp* index valuse for these days are presented in Table 1.

It can be seen that the electron density (N_e) from both descending orbits (day time) and ascending orbits (night time) during the magnetic storm significantly increased (red line in Figure 7) compared with N_e on other days. In day time (local time), the positive-phase was found initially in the mid-latitude with a small positive effect found in low-latitudes of the northern hemisphere (Figure 7a). The big positive phase then occurred in the equatorial region (Figure 7b). Later, the positive-phase decreased and finally disappeared (Figure 7c). In night time (local time), significant enhancement in the low-latitude and equatorial regions was obvious (Figure 7(d, e, f)). And the negative-phase was also found in the mid-latitude of the southern hemisphere at the same time (Figure 7(d, e)). In low latitudes, the maximum electron density at 02:00 LT (descending orbit) increased to 100% (Figure 7A), while the N_e at 14:00 LT (ascending orbit) increased to a maximum of 30% (Figure 7B). This is consistent with previous research findings (Buonsanto, 1999; Balan et al., 2010). It is noted that, for this magnetic storm, the asymmetry between the northern and southern hemispheres was clear. In June, the northern hemisphere is in summer and the southern hemisphere is in winter; the data in low and mid latitudes of the summer hemisphere display positive-phase, while negative-phase is observed in the winter hemisphere.

Furthermore, the response of N_e to the magnetic storm is sensitive especially in ascending orbits during nighttime. The N_e displays different disturbances according to different *Kp* value. Beside the most severe disturbance on the day of the magnetic storm (red line), the degree of disturbance varies with *Kp*, such as the blue line corresponding to *Kp* equal to 3, green line corresponding to 2, and then the yellow line and purple line (Figure 7A). But T_e did not show the same sensitivity as N_e.

The phenomenon observed during the storm is consistent with the basic laws of geomagnetic storm effect evolution; the phenomenon in day time is probably caused by neutral wind and penetrating electric field, and the one in night time is probably related to wind dynamo disturbance (Buonsanto, 1999). In this paper, we present just the LAP's responses to the magnetic storm objectively. We have not attempted to describe their physical mechanism in detail.

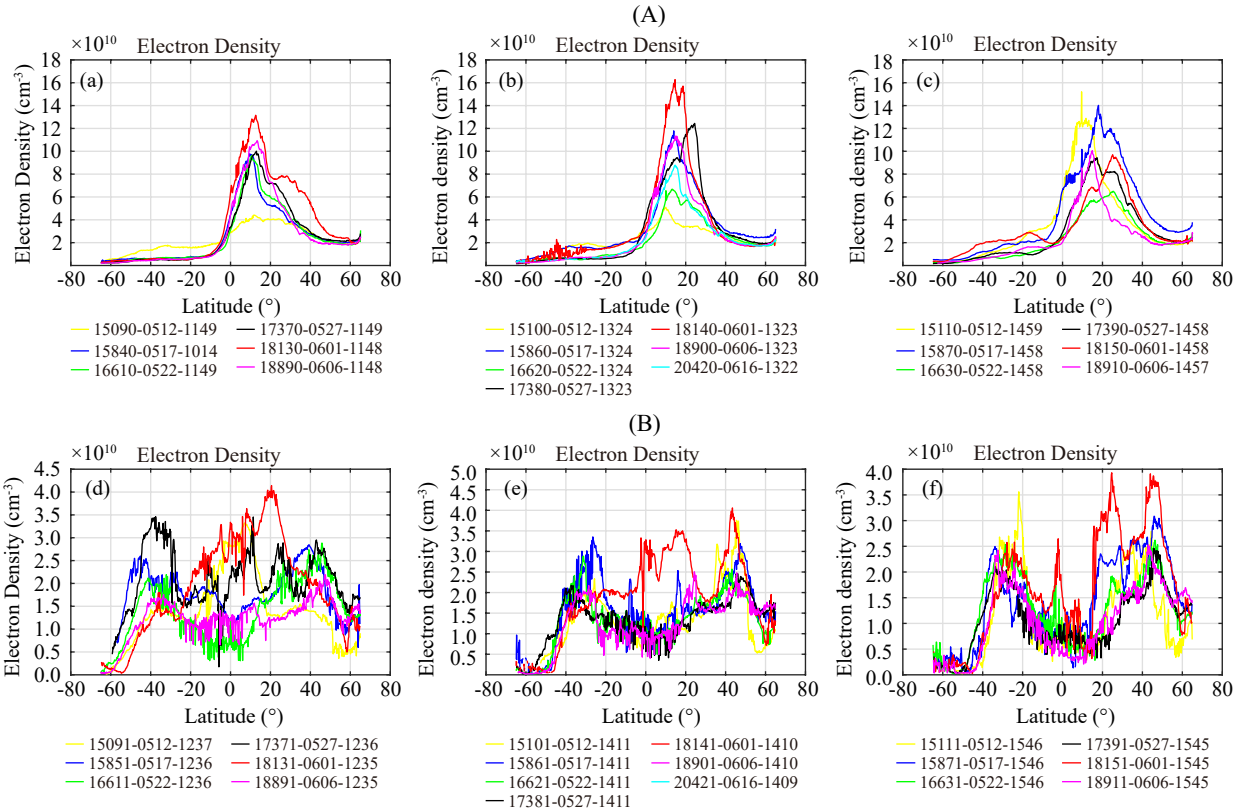

Figure 7. Changes in N_e obtained by CSES from 12 May to 16 June. The up panels (A) are Descending orbits (local time 14:00), including (a) orbit 18130 in 1 June and its revisited orbits, (b) orbit 18140 in 1 June and its revisited orbits, (c) orbit 18150 in 1 June and its revisited orbits; The bottom panels (B) are ascending orbits (local time 02:00), including (d) orbit 18131 in 1 June and its revisited orbits, (e) orbit 18141 in 1 June and its revisited orbits, (f) orbit 18151 in 1 June and its revisited orbits. Legend, such as '18130-0601-1148', means 'orbitnumber-date (mmdd)-time (hhmm)'.

4.2 M_s 6.9 Sumbawa, Indonesia Earthquake

The earthquake that occurred on 5 August 2018 in Sumbawa, Indonesia with a magnitude of 6.9 (116.452°E, 8.287°S), has been selected to study ionospheric perturbation in N_e and T_e during earthquakes.

The ionospheric perturbations were studied using the moving median method (MMM) on data from 10 days before and 2 days after this earthquake (in local time). MMM method reveals temporal variations before and after an earthquake and can remove the background effects effectively (Liu J et al., 2011, 2014; Priyadarshi et al., 2011; Liu J, 2013).

We adjusted some parameters according to the CSES data. The original data along one nighttime orbit around the epicenter ±10° were resampled by 0.5° in latitude direction, and then the current background median was calculated by applying the moving method to data from the previous 10 orbits (about 10 days) as the the calculation window and 1 orbit as the step window, taking 80% and 20% quintiles as the upper and lower thresholds, as shown in Figure 8a. Then we calculated the relative changes '*Dev*' (see Figure 8b). *Od, Ub,* and *Lb* are observational data, upper threshold and lower threshold respectively.

The *Dev* is (*Od*–*Ub*)/*Ub* when observation data are larger than the upper threshold, and *Dev*=(*Od*–*Lb*)/*Lb* if observation data are smaller than the lower threshold. If observation data fall between the upper and lower thresholds, the *Dev* is 0.

Figure 8a shows the variability of *Od, Bd, Ub* and *Lb* (from 23 July to 7 August) during the earthquake (*M*=6.8 and *M*=6.5). *Ub* and *Lb* are the upper and lower limits of day-to-day variability in ionospheric N_e. We have checked the *Kp* index around the epicenter during these times and all of them are less than or equal to 3. So this period is free from magnetic storm. In this case we observed the perturbation in N_e on the second day (3 August) and the sixth day (29 July) before the main seismic shock (5 August) when the N_e increased by more than 60%. It should be noted that there was another earthquake with magnitude of 6.5 on 28 July in nearly same position (116.55°E, 8.3°S). The increase on the sixth day before the M_s 6.8 earthquake is also on one day after the M_s 6.6 seismic shock (28 July). We can't give a definite conclusion whether the disturbance is a post-phenomenon of the M_s 6.5 earthquake or a pre-phenomenon of the M_s 6.8 earthquake. There are also two weak increases on July 24 and 25. However, according to previous study, we need not care about *Dev* less than 0.5 (Liu J, 2013). We did not observe any special phenomenon in T_e. The phenomenon observed in this paper is consistent with previous research results (Liu J et al., 2011, 2014; Priyadarshi et al., 2011; Liu J, 2013). We do not address the mechanism about LAI (Lithosphere-Atmosphere-Ionosphere) coupling (Pulinets et al., 2015) in this pa-

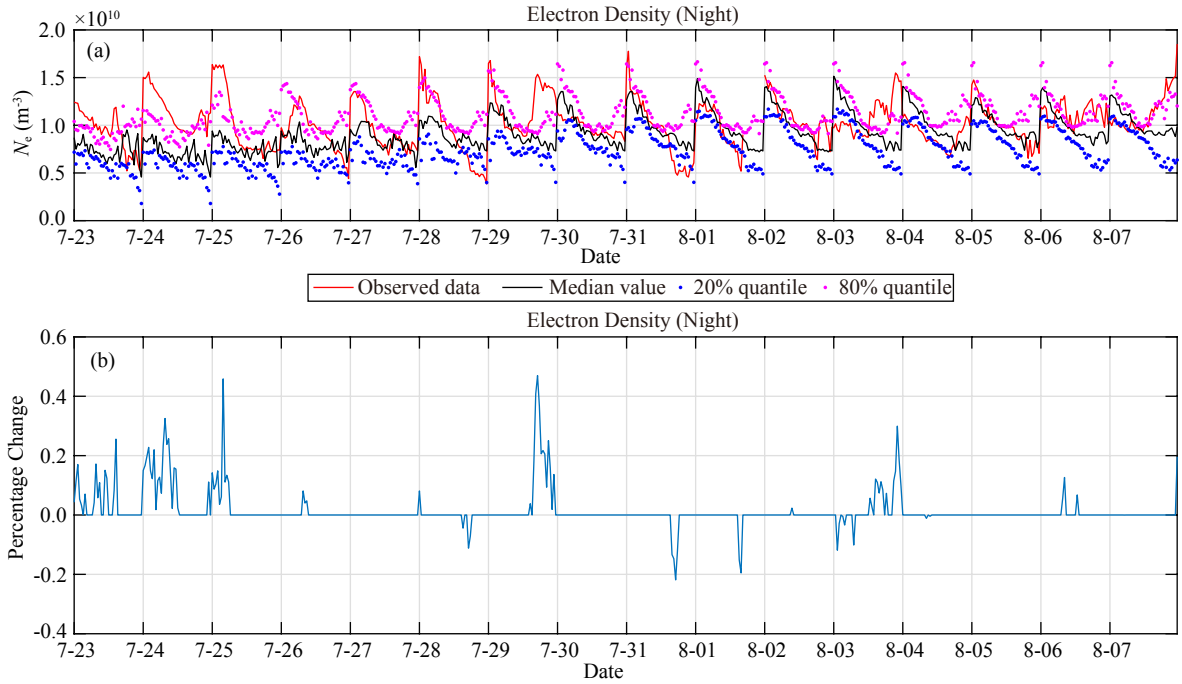

Figure 8. MMM analysis of Indonesia earthquake on August 5th, 2018. (a) The variation of observation data comparing to background data; (b) The variation of *Dev*. In panel (a), red, black and blue lines represent median value of observation data, median value of background data, upper and lower thresholds respectively; panel (b) shown the *Dev* values.

per. Further research will be performed using CSES data later.

5. Conclusions

The CSES Langmuir probe instrument (LAP) has been described and the main instrument operation modes are explained. The main plasma parameters that can be reliably extracted from the LAP current–voltage response are the electron temperature and density and the plasma potential. Variations of these parameters are obtained with a time resolution with a time resolution of 1.5 s (burst mode) and 3 s (survey mode).

The CSES is currently undergoing orbit-testing; data from the LAP may be either unavailable or subject to interference from CSES experiments or tests. Based on the data that were available, this paper studied magnetic storms and seismic events. Examples of these geophysical phenomena observed with the LAP illustrate the instrument's capabilities.

Improvements of data quality, perfection of data processing methods, and authenticity verification of data are still in progress. In the future, more scientific results will be obtained with further analysis of scientific data.

It is anticipated that a complete data set will be acquired over the lifetime of the CSES mission that will allow main CSES science objectives to be addressed in depth. The LAP may also provide a valuable data set for seismic and space weather-related ionospheric studies.

Acknowledgments

The authors thank J. P. Lebreton, the PI of ISL on DEMETER, for his important suggestions and guidance regarding the data analysis method. The authors also thank S. R. Zhang, the professor in MIT Haystack Observatory, for his important suggestions and guidance regarding the magnetic storm. This work was supported by the National Natural Science Foundation of China (41404058) and Beijing Natural Science Foundation (8184091). We thank GFZ for providing *Kp* index (https://www.gfz-potsdam.de/en/kp-index/).

References

Balan, N., Shiokawa, K., Otsuka, Y., Kikuchi, T., Vijaya Lekshmi, D., Kawamura, S., Yamamoto, M., and Bailey, G. J. (2010). A physical mechanism of positive ionospheric storms at low latitudes and midlatitudes. *J. Geophys. Res.*, *115*(A2), A02304. https://doi.org/10.1029/2009JA014515

Bering, E. A., Kelley, M. C., Mozer, F. S., and Fahleson, U. V. (1973). Theory and operation of the split Langmuir Probe. *Planet. Space Sci.*, *21*(11), 1983–2001. https://doi.org/10.1016/0032-0633(73)90128-1

Brace, L. H., Carignan, G. R., Findlay, J. A. (1971). Evaluation of ionospheric electron temperature measurements by cylindrical probes. *Space Res.*, *11*, 1079–1105.

Buonsanto, M. J. (1999). Ionospheric storms—a review. *Space Sci. Rev.*, *88*(3-4), 563–601. https://doi.org/10.1023/A:1005107532631

Chen, F. F., and Chang, J. P. (2002). *Principles of Plasma Processing* (pp. 2–8). New York: Plenum/Kluwer Publishers.

Eriksson, A. I., Boström, R., Gill, R., Åhlén, L., Jansson, S. E., Wahlund, J. E., André, M., Mälkki, A., Holtet, J. A., … The LAP Team. (2007). RPC-LAP: The Rosetta Langmuir Probe Instrument. *Space Sci. Rev.*, *128*(1-4), 729–744. https://doi.org/10.1007/s11214-006-9003-3

Godyak, V. A., and Alexandrovich, B. M. (2015). Comparative analyses of plasma probe diagnostics techniques. *J. Appl. Phys.*, *118*(23), 233302. https://doi.org/10.1063/1.4937446

Guan, Y. B., Wang, S. J., Liu, C., and Feng, Y. B. (2011). The design of the Langmuir probe onboard a seismo-electromagnetic satellite. In Proceedings of SPIE 8196, *International Symposium on Photoelectronic Detection and Imaging 2011: Space Exploration Technologies and Applications*. Beijing: SPIE. https://doi.org/10.1117/12.902308

He, Y., Yang, D. M., Zhu, R., Qian, J. D., and Parrot, M. (2010). Variations of electron density and temperature in ionosphere based on the DEMETER ISL data. *Earthq. Sci.*, *23*(4), 349–355. https://doi.org/10.1007/s11589-010-0732-8

He, Y., Yang, D., Qian, J., and Parrot, M. (2011). Response of the ionospheric electron density to different types of seismic events. *Nat. Hazards Earth Syst. Sci.*, *11*(8), 2173–2180. https://doi.org/10.5194/nhess-11-2173-2011

Holback, B., Jacksén, Å., Åhlén, L., Jansson, S. E., Eriksson, A. I., Wahlund, J. E., Carozzi, T., and Bergman, J. (2001). LINDA-the Astrid-2 Langmuir probe instrument. *Ann. Geophys.*, *19*(6), 601–610. https://doi.org/10.5194/angeo-19-601-2001

Hutchinson, I. H. (1987). *Principles of Plasma Diagnostics* (pp. 55–66). New York: Cambridge University Press.

Langmuir, I., and Mott-Smith, H. M. (1924). Studies of electric discharges in gases at low pressures. *Gen. Electr. Rev.*, *27*(7), 449–455.

Langmuir, I. (1932). Electric discharges in gases at low pressures. *J. Franklin Inst.*, *214*(3), 275–298. https://doi.org/10.1016/S0016-0032(32)90932-6

Lebreton, J. P., Stverak, S., Travnicek, P., Maksimovic, M., Klinge, D., Merikallio, S., Lagoutte, D., Poirier, B., Blelly, P. L., … Salaquarda, M. (2006). The ISL Langmuir probe experiment processing onboard DEMETER: Scientific objectives, description and first results. *Planet. Space Sci.*, *54*(5), 472–486. https://doi.org/10.1016/j.pss.2005.10.017

Li, M., and Parrot, M. (2012). "Real time analysis" of the ion density measured by the satellite DEMETER in relation with the seismic activity. *Nat. Hazards Earth Syst. Sci.*, *12*(9), 2957–2963. https://doi.org/10.5194/nhess-12-2957-2012

Liu, C., Guan, Y. B., Zhang, A. B., Zheng, X. Z., and Sun, Y. Q. (2016). The ionosphere measurement technology of Langmuir probe on China seismo-electromagnetic satellite. *Acta Phys. Sin.* (*in Chinese*), *65*(18), 189401. https://doi.org/10.7498/aps.65.189401

Liu, C., Guan, Y. B., Zheng, X. Z., Zhang, A. B., Piero, D., and Sun, Y. Q. (2018). The technology of space plasma in-situ measurement on the China Seismo-Electromagnetic Satellite. *Science China*. https://doi.org/http://engine.scichina.com/publisher/scp/journal/SCTS/doi/10.1007/s11431-018-9345-8?slug=abstract

Liu, J., Wan, W. X., Huang, J. P., Zhang, X. M., Zhao, S. F., Ouyang, X. Y., and Zeren, Z. M. (2011). Electron density perturbation before Chile *M*8.8 earthquake. *Chinese J. Geophys.* (*in Chinese*), *54*(11), 2717–2725. https://doi.org/10.3969/j.issn.0001-5733.2011.11.001

Liu, J. (2013). Ionopheric perturbance study before earthquakes [Ph. D. thesis] (in Chinese). Beijing: University of Chinese Academy of Sciences.

Liu, J., Huang, J. P., and Zhang, X. M. (2014). Ionospheric perturbations in plasma parameters before global strong earthquakes. *Adv. Space Res.*, *53*(5), 776–787. https://doi.org/10.1016/j.asr.2013.12.029

Mott-Smith, H. M. (1961). The theory of collectors in gaseous discharges. In Suits, C. G. (Ed.), *Electrical Discharge* (pp. 99–132). Amsterdam: Elsevier. https://doi.org/10.1016/B978-1-4831-9909-2.50013-8

Parrot, M. (2012). Statistical analysis of automatically detected ion density variations recorded by DEMETER and their relation to seismic activity. *Ann. Geophys.*, *55*(1), 149–155. https://doi.org/10.4401/ag-5270

Píša, D., Parrot, M., and Santolík, O. (2011). Ionospheric density variations recorded before the 2010 M_w 8.8 earthquake in Chile. *J. Geophys. Res.*, *116*(A8), A08309. https://doi.org/10.1029/2011JA016611

Priyadarshi, S., Kumar, S., and Singh, A. K. (2011). Ionospheric perturbations associated with two recent major earthquakes ($M > 5.0$). *Phys. Scr.*, *84*(4), 045901. https://doi.org/10.1088/0031-8949/84/04/045901

Pulinets, S. A., Ouzounov, D. P., Karelin, A. V., and Davidenko, D. V. (2015). Physical bases of the generation of short-term earthquake precursors: A complex model of ionization-induced geophysical processes in the lithosphere-atmosphere-ionosphere-magnetosphere system. *Geomagn. Aeron.*, *55*(4), 521–538. https://doi.org/10.1134/S0016793215040131

Sarkar, S., Gwal, A. K., and Parrot, M. (2007). Ionospheric variations observed by the DEMETER satellite in the mid-latitude region during strong earthquakes. *J. Atmos. Solar -Terr. Phys.*, *69*(13), 1524–1540. https://doi.org/10.1016/j.jastp.2007.06.006

Sarkar, S., Choudhary, S., Sonakia, A., Vishwakarma, A., and Gwal, A. K. (2012). Ionospheric anomalies associated with the Haiti earthquake of 12 January 2010 observed by DEMETER satellite. *Nat. Hazards Earth Syst. Sci.*, *12*(3), 671–678. https://doi.org/10.5194/nhess-12-671-2012

Shen, X. H., Zhang, X. M., Yuan, S. G., Wang, L. W., Cao, J. B., Huang, J. P., Zhu, X. H., Piergiorgio, P., and Dai, J. P. (2018). The state-of-the-art of the China Seismo-Electromagnetic Satellite mission. *Sci. China Technol. Sci.*, *61*(5), 634–642. https://doi.org/10.1007/s11431-018-9242-0

Szuszczewicz, E. P. (1972). Area influences and floating potentials in Langmuir probe measurements. *Journal of Applied Physics*, *43*(3), 874–880. https://doi.org/10.1063/1.1661297

Yan, R., Parrot, M., and Pinçon, J. L. (2017a). Statistical study on variations of the ionospheric ion density observed by DEMETER and related to seismic activities. *J. Geophys. Res.*: *Space Phys.*, *122*(12), 12421–12429. https://doi.org/10.1002/2017JA024623

Yan, R., Hu, Z., Wang, L. W., Guan, Y. B., and Liu, C. (2017b). Preliminary data inversion method of Langmuir probe onboard CSES. *Acta Seismol. Sin.* (*in Chinese*), *39*(2), 239–247. https://doi.org/10.11939/jass.2017.02.007

Yao, Y. B., Chen, P., Zhang, S., and Chen, J. J. (2013). Temporal and spatial variations in ionospheric electron density profiles over South Africa during strong magnetic storms. *Nat. Hazards Earth Syst. Sci.*, *13*(2), 375–384. https://doi.org/10.5194/nhess-13-375-2013

Zhang, X. M., Shen, X. H., Liu, J., Ouyang, X. Y., Qian, J. D., and Zhao, S. F. (2010a). Ionospheric perturbations of electron density before the Wenchuan Earthquake. *Int. J. Remote Sens.*, *31*(13), 3559–3569. https://doi.org/10.1080/01431161003727762

Zhang, X. M., Liu, J., Shen, X. H., Parrot, M., Qian, J. D., Ouyang, X. Y., Zhao, S. F., and Huang, J. P. (2010b). Ionospheric perturbations associated with the *M*8.6 Sumatra earthquake on 28 March 2005. *Chinese J. Geophys.* (*in Chinese*), *53*(3), 567–575. https://doi.org/10.3969/j.issn.0001-5733.2010.03.010

Zhao, G. Z., Chen, X. B., and Cai, J. T. (2007). Electromagnetic observation by satellite and earthquake prediction. *Prog. Geophys.* (*in Chinese*), *22*(3), 667–673. https://doi.org/10.3969/j.issn.1004-2903.2007.03.002